Editors' Suggestion | Featured in Physics

Evidence for PeV Proton Acceleration from Fermi-LAT Observations of SNR G106.3 + 2.7

Ke Fang,[1] Matthew Kerr,[2] Roger Blandford,[3,4] Henrike Fleischhack,[5,6,7] and Eric Charles[4,3]
[1]Department of Physics, Wisconsin IceCube Particle Astrophysics Center, University of Wisconsin, Madison, Wisconsin 53706, USA
[2]Space Science Division, Naval Research Laboratory, Washington, D.C. 20375, USA
[3]Kavli Institute for Particle Astrophysics and Cosmology, Stanford University, Stanford, California 94305, USA
[4]SLAC National Accelerator Laboratory, 2575 Sand Hill Road, Menlo Park, California 94025, USA
[5]Department of Physics, Catholic University of America, Washington, D.C. 20064, USA
[6]NASA Goddard Space Flight Center, Greenbelt, Maryland 20771, USA
[7]Center for Research and Exploration in Space Science and Technology, NASA/GSFC, Greenbelt, Maryland 20771, USA

(Received 22 December 2021; revised 8 March 2022; accepted 1 July 2022; published 10 August 2022)

The existence of a "knee" at energy ∼1 PeV in the cosmic-ray spectrum suggests the presence of Galactic PeV proton accelerators called "PeVatrons." Supernova remnant (SNR) G106.3 + 2.7 is a prime candidate for one of these. The recent detection of very high energy (0.1–100 TeV) gamma rays from G106.3 + 2.7 may be explained either by the decay of neutral pions or inverse Compton scattering by relativistic electrons. We report an analysis of 12 years of Fermi-LAT gamma-ray data that shows that the GeV-TeV gamma-ray spectrum is much harder and requires a different total electron energy than the radio and x-ray spectra, suggesting it has a distinct, hadronic origin. The nondetection of gamma rays below 10 GeV implies additional constraints on the relativistic electron spectrum. A hadronic interpretation of the observed gamma rays is strongly supported. This observation confirms the long-sought connection between Galactic PeVatrons and SNRs. Moreover, it suggests that G106.3 + 2.7 could be the brightest member of a new population of SNRs whose gamma-ray energy flux peaks at TeV energies. Such a population may contribute to the cosmic-ray knee and be revealed by future very high energy gamma-ray detectors.

DOI: 10.1103/PhysRevLett.129.071101

G106.3 + 2.7 is a comet-shaped, middle-aged (∼10 kyr) SNR at a distance of ∼800 pc [1,2]. In the radio and x-ray bands, it is composed of a small "head" structure in the north and an extended "tail" in the southwest with lower surface brightness. The pulsar PSR J2229 + 6114 and its wind nebula, the "Boomerang" (with a length of about 3'), are located at the northern edge of the head (see Fig. 1) and are conjectured to result from the same supernova explosion that led to the formation of G106.3 + 2.7 [2]. Nonthermal diffuse x-ray emission [3,4] and radio emission [2] are detected from the entire SNR. The intensity in both bands increases toward PSR J2229 + 6114 [1,3,4]. The radio and x-ray spectra from XMM-Newton and Chandra are found to be harder in the head than in the tail [1,3], though an analysis of the Suzaku data concludes that the photon index does not change with the distance from the pulsar [4].

The very high energy (VHE; 0.1–100 TeV) gamma-ray emission of the SNR appears to come from the tail [32–35]. The 68% extension of the VHE emission is measured to be 0.23°–0.45° by different experiments, though the values are consistent within uncertainties. The centroids of gamma-ray emission regions measured by VERITAS and Tibet and the best-fit position found by LHAASO overlap with a molecular cloud, while the VHE emission region in the HAWC data is consistent with both the pulsar and the molecular cloud due to the large position uncertainty. When modeling the VHE counts rate spectrum (photons $\mathrm{eV}^{-1}\,\mathrm{cm}^{-2}\,\mathrm{s}^{-1}$) as a power law, $dN/dEdAdt \propto E^{-\alpha}$, the best-fit spectral index α is found between 2.3 and 3.0. The observed spectrum and the morphology may be explained by the interaction of hadronic cosmic rays and the molecular cloud, but a leptonic scenario, where gamma rays are produced by locally accelerated relativistic electrons, is still possible [32–34].

High-energy (0.1–100 GeV) gamma-ray observations, especially below 10 GeV, are crucial to breaking the degeneracy of the hadronic and leptonic scenarios. A previous analysis [36] using 10 years of Fermi-LAT data above 3 GeV found an excess in the tail with a test statistic (TS) [37] of 35.5 and a disk morphology of radius 0.25°, while the properties of G106.3 + 2.7 below 3 GeV remained unexplored. Such low-energy analysis is complicated because PSR J2229 + 6114, also known as 4FGL J2229.0 + 6114 in the fourth Fermi-LAT catalog of gamma-ray sources (4FGL-DR2 [38,39]), dominates the gamma-ray emission of the entire region up to a few GeV as explained in the Supplemental Material [8].

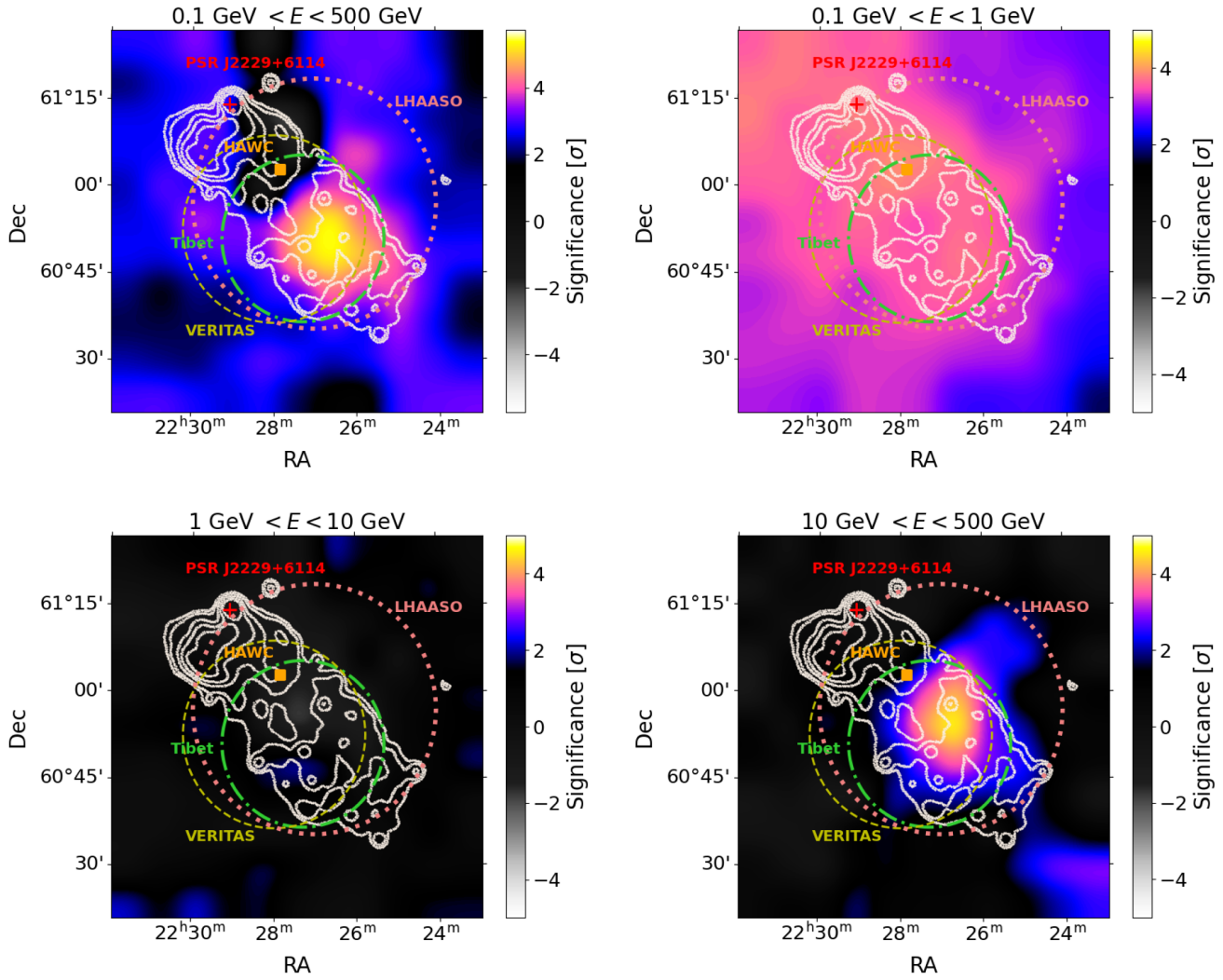

FIG. 1. Residual significance maps of the G106.3 + 2.7 region computed using the method of [5] from the analysis of 12 years of 0.1–500 GeV Fermi-LAT [6] data (top left) and divided into three energy bins: 0.1–1 GeV (top right), 1–10 GeV (bottom left), and > 10 GeV (bottom right). All maps except the > 10 GeV one were computed using the weighted likelihood analysis [7] and phase-gated data (see the Supplemental Material [8]), while the > 10 GeV analysis used all of the data. The color scale indicates the statistical significance of a deviation between the data and the source model, evaluated on a grid with 0.1° × 0.1° spacing. The maps are smoothed by Gaussian interpolation. For comparison, we show the radio continuum emission at 1420 MHz [2] (white contours), the position of the pulsar PSR J2227 + 6114 (red plus marker), the point source detected by HAWC [32] (orange square marker), and extended gamma-ray emitting regions observed by VERITAS [33] (yellow dashed circle), Tibet ASγ [34] (green dash-dotted circle), and LHAASO [35] (coral dotted circle).

Results of the Fermi-LAT analysis.—We searched for high-energy gamma-ray signals using 12 years of Fermi-LAT data selected to include only rotational phases when the gamma-ray emission of the pulsar is minimal to avoid this background contamination. By eliminating 50% of the observing time, we reduce the background from PSR J2229 + 6114 by > 95% at low energies (0.1 GeV) and by 99% above 1 GeV (details are provided in Figs. S1 and S2 in the Supplemental Material [8]). Figure 1 presents the maps of the significance of the deviations between the LAT data and the source model, comprising sources in the 4FGL-DR2 catalog [39] and diffuse backgrounds, in the full energy range and three energy bins: 0.1–1 GeV, 1–10 GeV, and above 10 GeV. The deviation significance is computed according to [5], applying for each pixel an energy-dependent spatial selection that roughly follows the LAT point-spread function (PSF). Such maps allow us to detect potential excess emissions (pointlike or with a relatively small, degree-scale extension, as explained in the Supplemental Material [8]), whose spatial and spectral characteristics are subsequently investigated with a more detailed analysis, as explained below. In the lowest-energy bin, excess emission is present in the entire vicinity of the remnant with low significance. As the 68% containment

radius of the PSF of the LAT below 1 GeV is larger than 2°, the photons may also come from nearby sources or the Galactic plane. In the intermediate energy bin, no significant excess or deficit is observed inside the remnant. A source is clearly present in the highest-energy bin, with the best-fit position consistent with the VHE gamma-ray emitting site.

Above 10 GeV, the pulsar emission is negligible, and the 68% containment radius of the PSF of the LAT ($\lesssim 0.2°$) is narrower than the angular distance between the pulsar and the gamma-ray emitting site, so we use all the data for the analysis. When fitting the data with a point-source morphology and a power-law energy distribution, we obtain TS = 36.5 with four free parameters, including the coordinates of the source position, and the flux normalization and spectral index. This corresponds to 5.2σ standard deviations. The best-fit spectral index is 1.72 ± 0.20 and the maximum likelihood coordinates are $(\mathrm{RA}, \mathrm{Dec}) = (336.71° \pm 0.03°, 60.90° \pm 0.03°)$ (J2000), corresponding to Galactic coordinates $(l, b) = (106.24° \pm 0.03°, 2.81° \pm 0.03°)$. The position and the differential energy flux of the emission are consistent with those found in the TeV measurements. We also fit the data with extended spatial profiles and summarize the results in the Supplemental Material [8]. In general an extended morphology yields a larger TS since the extended model has one more degree of freedom than the point-source model. The most favored extended model with a Gaussian radial profile yields $\Delta\mathrm{TS} = 7.4$ with 0.2° radius, which is not a significant improvement over the point-source model ($< 3\sigma$). We thus conclude that gamma-ray emission from G106.3 + 2.7 is unresolved in the LAT data above 10 GeV.

We then use these > 10 GeV results to guide the analysis above 0.1 GeV, where the angular resolution is poorer and the diffuse background emission is larger. To reduce the impact of diffuse emission below ~3 GeV, we maximize a likelihood function that includes deweighting the photons in that energy range [7]. Using the phase-gated data, fixing the G106.3 + 2.7 position to the best-fit values found in the > 10 GeV analysis, and leaving the spectral parameters of the SNR free, we find a TS of 20.8 with a point-source morphology and 34.8 with a 2D Gaussian template with 68% containment radius of 0.2°, corresponding to 4.2σ and 5.6σ standard deviations, respectively. Below we take the extended template as a benchmark model that provides the greatest likelihood of the SNR among the models that we studied. The blue data points in Fig. 2 show the spectral energy distribution (SED) of the SNR from the fit results from the benchmark model. The SED is calculated by binning the photons into four bins per decade in energy and performing a weighted likelihood analysis in each energy bin. For all spatial templates we tested, no significant emission is detected below 10 GeV.

Since the SNR is not bright, the measured flux may be affected by the modeling of nearby faint emission regions.

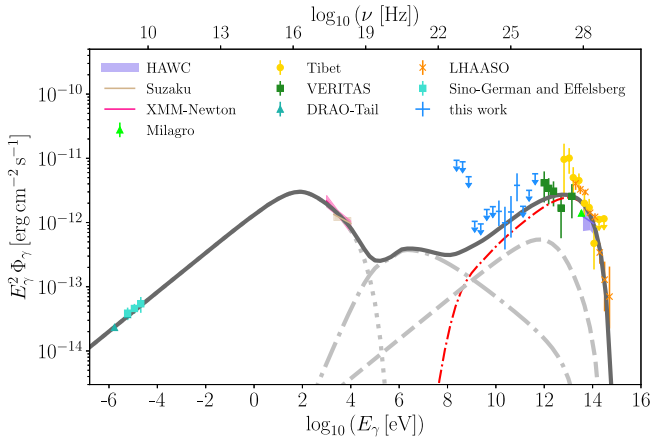

FIG. 2. Broadband spectral energy distribution of supernova remnant G106.3 + 2.7. The multiwavelength data include radio [1,40], x-ray [3,4], and VHE gamma ray [32–35]. Error bars indicate 1σ uncertainties. For the LAT data points, 95% upper limits are shown when TS < 4, otherwise 1σ error bars are shown. The VERITAS flux points are scaled up by a factor of 1.62 from the original values to account for the gamma-ray signals outside the signal extraction region of the analysis [33,34]. For comparison, the multiwavelength spectrum from a hybrid model including an electron population (in gray color) and a proton population (in red color) is shown. The injection spectra of both populations are assumed to be exponentially cut off power laws (refer to the text for the best-fit values of the spectral parameters). The electrons produce radio to x-ray photons through synchrotron emission in a magnetic field (dotted curve), hard x-ray to sub-GeV gamma ray through Bremsstrahlung emission with gas in the interstellar medium (dash dotted curve), and gamma rays above 10 GeV through inverse Compton scattering of the CMB (dashed curve). The protons produce gamma rays through gas interaction (dash-dotted curve).

We discuss this impact in the Supplemental Material [8], but note that transferring more of the GeV emission from the SNR to any background source than in the benchmark model only strengthens the evidence, discussed below, for the presence of protons accelerated by SNR G106.3 + 2.7.

Multiwavelength observation and broadband SED.—We combine the Fermi-LAT spectral results with the radio, x-ray, and VHE observations of the remnant and use the broadband SED to constrain physical models through the Markov chain Monte Carlo technique. Nested models are then compared using both the likelihood-ratio test and the Bayesian information criterion (BIC) [41]. Since Wilks' theorem [42] applies only to nested models, our comparisons of other models are based only on BIC values.

Physical models of VHE gamma-ray emission invoke high-energy leptons, hadrons, or a combination of the two. In the one-component leptonic version, a population of relativistic electrons is continuously injected by either the magnetosphere or the nebula of the pulsar, or the supernova remnant shock front. The electrons are confined by magnetic turbulence over the source age $t_{\mathrm{age}} \sim 10$ kyr

and cool through synchrotron, bremsstrahlung, and inverse Compton radiation. The electron spectrum can be modeled by a power-law spectrum with an exponential cutoff, $dN_e/dE = N_{e0}\gamma^{-\alpha_e}\exp(-E/E_{e\,\max})$, where $\gamma = E/m_e c^2$ is the Lorentz factor. To calculate the flux of the bremsstrahlung radiation, we adopt a gas density equal to the average interstellar medium density, $n_{\rm gas} = 1\ {\rm cm}^{-3}$. This mean density is supported by the presence of H I and CO gas associated with the SNR [2], and $n_{\rm gas}$ would be much greater at the location of the molecular cloud [34,43]. The value is consistent with the expected SNR gas density in the Taylor-Sedov phase [44,45], $n_{\rm Sedov} \sim 2.1(E_{\rm exp}/10^{51}\ {\rm erg})\times(t_{\rm age}/10\ {\rm kyr})^2({\rm R}/10\ {\rm pc})^{-5}\ {\rm cm}^{-3}$, where $E_{\rm exp}$ is the total energy released by the supernova explosion and R is the size of the SNR. As no conspicuous infrared emission is found from the SNR [2], the inverse Compton radiation is calculated using the cosmic microwave background (CMB) and a background Galactic far infrared emission with temperature 30 K and energy density $0.3\ {\rm eV\,cm}^{-3}$ [46] as the target radiation background. The electron spectrum is obtained by numerically solving the transport equation assuming a continuous injection as described in the Supplemental Material [8]. The top panel of Fig. S5 presents the best-fit one-component leptonic model. We find that the leptonic model fails to explain the multiwavelength emission for two main reasons. First, the radio and nonthermal x-ray emission suggests an electron spectral index $\alpha_e = 2.42^{+0.04}_{-0.06}$, whereas a harder electron spectrum with $\alpha_e = 2.14^{+0.09}_{-0.11}$ is needed to explain the gamma-ray flux from sub-GeV to a few TeV. The best-fit electron spectrum based on the radio to x-ray data has a total energy $W_e \sim 10$ times higher than the W_e derived from the gamma-ray data. The differences in α_e and W_e are smaller in a less physical model where the cooling of electrons is not included. Second, the bremsstrahlung emission by low-energy and high-energy electrons appears at the energy ranges where the end of the synchrotron emission and the beginning of the inverse Compton emission also contribute. Together, these components are in tension with the x-ray measurements at 2–10 keV and the 1–10 GeV Fermi-LAT upper limits, respectively. As a result, the best-fit model flux is 5–10 times lower than the measured flux above 100 TeV. The tension would be stronger if $n_{\rm gas}$ is higher than $1\ {\rm cm}^{-3}$.

By contrast, a similarly simple hybrid model that includes a hadronic contribution naturally accounts for these spectral features. The proton spectrum can be modeled by a single power-law spectrum with an exponential cutoff, $dN_p/dE = N_{p0}\gamma^{-\alpha_p}\exp(-E/E_{p\,\max})$, where $\gamma = E/m_p c^2$ is the Lorentz factor of protons. The relativistic protons interact with gas in the surrounding medium and produce neutral pions that decay into gamma rays. Figure 2 shows the best-fit model with the following parameters: $\log(N_{p0}/{\rm eV}^{-1}) = 40.27^{+0.50}_{-0.77}$, $\alpha_p = 1.73^{+0.12}_{-0.16}$, $\log(E_{p,\max}/{\rm eV}) = 14.95^{+0.13}_{-0.13}$, $\log(N_{e0}/{\rm eV}^{-1}) = 47.69^{+0.57}_{-0.53}$, $\alpha_e = 2.39^{+0.05}_{-0.06}$, $\log(E_{e,\max}/{\rm eV}) = 14.54^{+0.26}_{-0.15}$, and $B = 8.99^{+4.85}_{-3.54}\ \mu{\rm G}$. By integrating the energy flux EdN/dE above the rest masses of electrons and protons, we find a total proton energy $W_p = 3.3\times10^{48}$ erg and electron injection energy $W_e = 5.3\times10^{47}$ erg, respectively. The required particle acceleration efficiency, $\epsilon_{\rm CR} \sim (W_e + W_p)/E_k = 0.4\%(E_k/10^{51}\,{\rm erg})^{-1}$ with E_k being the kinetic energy of the SNR, can be achieved by a typical SNR. The ratio of the proton and electron acceleration efficiencies is $W_p/W_e \sim 10$, which is consistent with the finding from individual SNR observation and collectively in the cosmic-ray spectrum that SNRs accelerate protons ~10–100 times more efficiently than electrons [47]. The hybrid model is significantly preferred over the one-component leptonic model by $\Delta{\rm BIC} = -20.6$, and ${\rm TS} = 31.7$, which corresponds to 5.0σ.

We further investigate whether a more complicated leptonic model could better explain the data. Figure S5 shows such a model where two populations of electrons are invoked to resolve the difficulty of the one-component model in explaining the radio to x-ray and gamma-ray measurements simultaneously. The two components are assumed to be accelerated by different mechanisms, such as the pulsar and remnant shocks, and thus have different spectra. The two populations of electrons are assumed to both contribute to the tail region. This model is, however, again disfavored by data. The lepto-hadronic hybrid model yields a much lower BIC, $\Delta{\rm BIC} = -20.1$, compared to the two-component leptonic model, suggesting that it is significantly preferred. Moreover, as the radio and x-ray intensities are observed to span the entire remnant with their fluxes increasing toward the pulsar in a similar way, they likely share the same production mechanism. The two-component leptonic model would break down the natural connection of the two bands.

Besides poorer fits to data, leptonic models share a common weakness. If the x-ray and gamma-ray fluxes come from the synchrotron and inverse-Compton emission of electrons, respectively, the magnetic energy density of the SNR would be comparable to the energy density of the radiation field. Since gamma rays above 10 TeV are mostly upscattered CMB photons, the field strength cannot be much higher than ~3 μG. Such a field strength is too low for the acceleration of near-PeV electrons, which are needed to produce 100–500 TeV gamma rays. The maximum electron energy that can be accelerated by the remnant shocks is [48] $E_{e,\max} = 188\ {\rm TeV}\,\eta^{1/2}(B/3\ \mu{\rm G})^{-1/2}(v_{\rm sh}/3000\ {\rm kms}^{-1})$, where $v_{\rm sh}$ is the shock velocity and $\eta = \delta B^2/B^2$ is the degree of magnetic field fluctuations that characterizes the acceleration efficiency. Such a low field does not support an electron acceleration by the pulsar or its nebula. Because in that case, as the physical condition of the gamma-ray emitting site is not much different from the average

interstellar medium condition [49], GeV gamma rays should have been found in the head region of G106.3 + 2.7.

Summary and discussion.—SNRs have long been proposed as efficient accelerators of cosmic rays [45,50] up to PeV energies [51]. However, only a handful [52,53], out of hundreds of radio-emitting SNRs, have been observed to emit VHE radiation with a hard spectrum. The scarcity of PeVatron candidates and the rareness of SNRs with VHE emissions make SNR G106.3 + 2.7 a unique source. Our study provides strong evidence for proton acceleration in this nearby SNR, and by extension, supports a potential role for G106.3 + 2.7-like SNRs in meeting the challenge of accounting for the observed cosmic-ray knee using Galactic sources. Future VHE gamma-ray observatories such as Cherenkov Telescope Array [54] and Southern Wide-field Gamma-ray Observatory [55] could reveal the subgroup of SNRs that has gamma-ray energy flux peaked at TeV energies like G106.3 + 2.7.

The Fermi-LAT Collaboration acknowledges support for LAT development, operation, and data analysis from NASA and DOE (United States), CEA/Irfu and IN2P3/CNRS (France), ASI and INFN (Italy), MEXT, KEK, and JAXA (Japan), and the K. A. Wallenberg Foundation, the Swedish Research Council, and the National Space Board (Sweden). Science analysis support in the operations phase from INAF (Italy) and CNES (France) is also gratefully acknowledged. This work performed in part under DOE Contract No. DE-AC02-76SF00515. We thank Seth Digel for helpful comments on the manuscript. We thank Philippe Bruel for useful suggestions regarding the usage of PS maps. The work of K. F. is supported by the Office of the Vice Chancellor for Research and Graduate Education at the University of Wisconsin-Madison with funding from the Wisconsin Alumni Research Foundation. K. F. acknowledges support from NASA through the Fermi Guest Investigator Program (NNH19ZDA001N-FERMI, NNH20ZDA001N-FERMI) and from National Science Foundation (PHY-2110821). Work at N. R. L. is supported by NASA. H. F. acknowledges support by NASA under Grant No. 80GSFC21M0002.

[1] S. Pineault and G. Joncas, G106.3 + 2.7: A supernova remnant in a late stage of evolution, Astron. J. **120**, 3218 (2000).
[2] R. Kothes, B. Uyaniker, and S. Pineault, The supernova remnant G106.3 + 2.7 and its pulsar-wind nebula: Relics of triggered star formation in a complex environment, Astrophys. J. **560**, 236 (2001).
[3] C. Ge, R.-Y. Liu, S. Niu, Y. Chen, and X.-Y. Wang, Revealing a peculiar supernova remnant G106.3 + 2.7 as a petaelectronvolt proton accelerator with x-ray observations, Innovation **2**, 100118 (2021).
[4] Y. Fujita, A. Bamba, K. K. Nobukawa, and H. Matsumoto, X-ray emission from the PeVatron-candidate supernova remnant G106.3 + 2.7, Astrophys. J. **912**, 133 (2021).
[5] P. Bruel, A new method to perform data-model comparison in Fermi-LAT analysis, Astron. Astrophys. **656**, A81 (2021).
[6] W. B. Atwood, A. A. Abdo, M. Ackermann, W. Althouse, B. Anderson *et al.*, The Large Area Telescope on the Fermi Gamma-ray Space Telescope Mission, Astrophys. J. **697**, 1071 (2009).
[7] F. Acero, M. Ackermann, M. Ajello, A. Albert, W. B. Atwood *et al.* (Fermi-LAT Collaboration), Fermi Large Area Telescope Third Source Catalog, Astrophys. J. Suppl. Ser. **218**, 23 (2015).
[8] See Supplemental Material, which includes Refs. [8–30], at http://link.aps.org/supplemental/10.1103/PhysRevLett.129.071101 for further information about the data analysis and a more detailed description of physical models.
[9] W. Atwood, A. Albert, L. Baldini, M. Tinivella, J. Bregeon *et al.*, Pass 8: Toward the full realization of the Fermi-LAT scientific potential, arXiv:1303.3514.
[10] P. Bruel, T. H. Burnett, S. W. Digel, G. Johannesson, N. Omodei, and M. Wood, Fermi-LAT improved Pass ~8 event selection, arXiv:1810.11394.
[11] https://fermi.gsfc.nasa.gov/ssc/data/access/lat/BackgroundModels.html.
[12] J. R. Mattox *et al.*, The likelihood analysis of EGRET data, Astrophys. J. **461**, 396 (1996).
[13] M. Kerr, P. S. Ray, S. Johnston, R. M. Shannon, and F. Camilo, Timing gamma-ray pulsars with the Fermi Large Area Telescope: Timing noise and astrometry, Astrophys. J. **814**, 128 (2015).
[14] J. Luo, S. Ransom, P. Demorest, P. S. Ray, A. Archibald, M. Kerr, R. J. Jennings, M. Bachetti, R. van Haasteren, C. A. Champagne, J. Colen, C. Phillips, J. Zimmerman, K. Stovall, M. T. Lam, and F. A. Jenet, PINT: A modern software package for pulsar timing, Astrophys. J. **911**, 45 (2021).
[15] https://fermi.gsfc.nasa.gov/ssc/data/access/lat/ephems/.
[16] https://fermi.gsfc.nasa.gov/ssc/data/analysis/user/.
[17] V. Zabalza, naima: A Python package for inference of relativistic particle energy distributions from observed nonthermal spectra, Proc. Sci., ICRC2015 (**2015**) 922 [arXiv:1509.03319].
[18] K. Burnham and D. Anderson, Model Selection and Multimodel Inference (Springer, New York, 2002).
[19] R. Moderski, M. Sikora, P. S. Coppi, and F. Aharonian, Klein-Nishina effects in the spectra of non-thermal sources immersed in external radiation fields, Mon. Not. R. Astron. Soc. **363**, 954 (2005).
[20] M. Fiori, B. Olmi, E. Amato, R. Bandiera, N. Bucciantini, L. Zampieri, and A. Burtovoi, Modeling the γ -ray pulsar wind nebulae population in our galaxy, Mon. Not. R. Astron. Soc. **511**, 1439 (2022).
[21] V. S. Berezinskii, S. V. Bulanov, V. A. Dogiel, and V. S. Ptuskin, Astrophysics of Cosmic Rays (North Holland, 1990).
[22] M. V. Zombeck, *Handbook of Space Astronomy and Astrophysics*, 3rd ed. (Cambridge University Press, Cambridge, England, 2006).
[23] J. W. Norbury and L. W. Townsend, Parameterized total cross sections for pion production in nuclear collisions, Nucl. Instrum. Methods Phys. Res., Sect. B **254**, 187 (2007).

[24] K. Olive, Review of particle physics, Chin. Phys. C **40**, 100001 (2016).

[25] E. Kafexhiu, F. Aharonian, A. M. Taylor, and G. S. Vila, Parametrization of gamma-ray production cross sections for pp interactions in a broad proton energy range from the kinematic threshold to PeV energies, Phys. Rev. D **90**, 123014 (2014).

[26] A. Achterberg, R. Blandford, and V. Periwal, Two-fluid models of cosmic ray shock acceleration, Astron. Astrophys. **132**, 97 (1984).

[27] P. Blasi, S. Gabici, and G. Vannoni, On the role of injection in kinetic approaches to non-linear particle acceleration at non-relativistic shock waves, Mon. Not. R. Astron. Soc. **361**, 907 (2005).

[28] V. N. Zirakashvili and F. A. Aharonian, Nonthermal radiation of young supernova remnants: The case of RX J1713.7-3946, Astrophys. J. **708**, 965 (2010).

[29] T. Inoue, R. Yamazaki, S.-i. Inutsuka, and Y. Fukui, Toward understanding the cosmic-ray acceleration at young supernova remnants interacting with interstellar clouds: Possible applications to RX J1713.7-3946, Astrophys. J. **744**, 71 (2012).

[30] S. Gabici and F. A. Aharonian, Hadronic gamma-rays from RX J1713.7-3946?, Mon. Not. R. Astron. Soc. **445**, L70 (2014).

[31] S. Celli, G. Morlino, S. Gabici, and F. A. Aharonian, Supernova remnants in clumpy media: Particle propagation and gamma-ray emission, Mon. Not. R. Astron. Soc. **487**, 3199 (2019).

[32] A. Albert, R. Alfaro, C. Alvarez, J. R. A. Camacho, J. C. Arteaga-Velázquez *et al.* (HAWC Collaboration), HAWC J2227 + 610 and its association with G106.3 + 2.7, a new potential Galactic PeVatron, Astrophys. J. Lett. **896**, L29 (2020).

[33] V. A. Acciari, E. Aliu, T. Arlen *et al.*, Detection of extended VHE gamma-ray emission from G106.3 + 2.7 with VERITAS, Astrophys. J. **703**, L6 (2009).

[34] M. Amenomori, Y. Bao, X. J. Bi, D. Chen, T. L. Chen, W. Y. Chen *et al.* (Tibet ASγ Collaboration), Potential PeVatron supernova remnant G106.3 + 2.7 seen in the highest-energy gamma rays, Nat. Astron. **5**, 460 (2021).

[35] Z. Cao, F. Aharonian, Q. An *et al.*, Ultrahigh-energy photons up to 1.4 petaelectronvolts from 12 gamma-ray Galactic sources, Nature (London) **594**, 33 (2021).

[36] Y. Xin, H. Zeng, S. Liu, Y. Fan, and D. Wei, VER J2227 + 608: A hadronic PeVatron pulsar wind nebula?, Astrophys. J. **885**, 162 (2019).

[37] The test statistic is defined as $\mathrm{TS} = -2\log(\mathcal{L}_{\mathrm{max},0}/\mathcal{L}_{\mathrm{max},1})$, where $\mathcal{L}_{\mathrm{max},0,1}$ are maximum likelihood values for models without and with an additional source.

[38] Fermi-LAT Collaboration, Fermi Large Area Telescope Fourth Source Catalog, Astrophys. J. Suppl. Ser. **247**, 33 (2020).

[39] J. Ballet, T. H. Burnett, S. W. Digel, and B. Lott (Fermi-LAT Collaboration), Fermi Large Area Telescope Fourth Source Catalog Data Release 2, arXiv:2005.11208.

[40] X. Y. Gao, J. L. Han, W. Reich, P. Reich, X. H. Sun, and L. Xiao, A Sino-German λ6 cm polarization survey of the galactic plane. V. Large supernova remnants, Astron. Astrophys. **529**, A159 (2011).

[41] G. Schwarz, Estimating the dimension of a model, Ann. Stat. **6**, 461 (1978).

[42] S. S. Wilks, The large-sample distribution of the likelihood ratio for testing composite hypotheses, Ann. Math. Stat. **9**, 60 (1938).

[43] M. H. Heyer, C. Brunt, R. L. Snell, J. E. Howe, F. P. Schloerb, and J. M. Carpenter, The Five College Radio Astronomy Observatory CO survey of the outer galaxy, Astrophys. J. Suppl. Ser. **115**, 241 (1998).

[44] L. I. Sedov, *Similarity and Dimensional Methods in Mechanics* (Academic Press, 1959).

[45] S. P. Reynolds, Supernova remnants at high energy, Annu. Rev. Astron. Astrophys. **46**, 89 (2008).

[46] S. Vernetto and P. Lipari, Absorption of very high energy gamma rays in the Milky Way, Phys. Rev. D **94**, 063009 (2016).

[47] P. Blasi, The origin of galactic cosmic rays, Astron. Astrophys. Rev. **21**, 70 (2013).

[48] R. Blandford and D. Eichler, Particle acceleration at astrophysical shocks: A theory of cosmic ray origin, Phys. Rep. **154**, 1 (1987).

[49] R. Beck, Galactic and extragalactic magnetic fields, Space Sci. Rev. **99**, 243 (2001).

[50] D. Caprioli, Understanding hadronic gamma-ray emission from supernova remnants, J. Cosmol. Astropart. Phys. 05 (2011) 026.

[51] A. R. Bell, K. M. Schure, B. Reville, and G. Giacinti, Cosmic-ray acceleration and escape from supernova remnants, Mon. Not. R. Astron. Soc. **431**, 415 (2013).

[52] H. Abdalla, A. Abramowski, F. Aharonian, F. Ait Benkhali, E. O. Angüner *et al.* (H. E. S. S. Collaboration), Population study of galactic supernova remnants at very high γ-ray energies with H.E.S.S., Astron. Astrophys. **612**, A3 (2018).

[53] H. Fleischhack, A survey of TeV emission from galactic supernova remnants with HAWC, in *Proceedings of the 36th International Cosmic Ray Conference, ICRC2019, Madison, WI* (2019), Vol. 36, p. 674, arXiv:1907.08575.

[54] B. S. Acharya, I. Agudo, I. Al Samarai, R. Alfaro, J. Alfaro *et al.* (Cherenkov Telescope Array Consortium), *Science with the Cherenkov Telescope Array* (World Scientific, 2019).

[55] P. Abreu, A. Albert, R. Alfaro, C. Alvarez, R. Arceo, P. Assis *et al.*, The Southern Wide-Field Gamma-Ray Observatory (SWGO): A next-generation ground-based survey instrument, Bull. Am. Astron. Soc. **51**, 109 (2019).